Gong *et al. Chin. J. Mech. Eng.* (2019) 32:102
https://doi.org/10.1186/s10033-019-0413-z

Chinese Journal of Mechanical Engineering

ORIGINAL ARTICLE

Open Access

A Numerical Method for Extrication Characteristics of TBM Cutter-Head with the HVC

Huasheng Gong, Haibo Xie* and Huayong Yang

Abstract

Achieving highly efficient extrication of the tunnel boring machine (TBM) cutter-head driving system from the collapsed surrounding rock has become a key problem globally, and significant effort has been directed to improve TBM cutter-head extricating ability. In this study, the characteristics of a hydro-viscous device have been investigated to improve extricating performance of the TBM cutter-head. A numerical method based on an explicit pressure-linked equation is presented for computing the film parameters of the HVC, which is then applied to investigate extrication characteristics of a TBM cutter-head with a hydro-viscous clutch (HVC). The explicit pressure-linked equation is derived from the Navier–Stokes equations and the conservation equation, where boundary conditions are involved. The model of a cutter-head driving system with an HVC is established, and the extrication characteristics of the cutter-head driving system are analyzed and compared with three extrication strategies. The variation in extrication torque shows that the linear strategy or positive parabolic strategy are preferred for their relatively high extrication efficiency and low rigid impact, and the effects of throughflow rate on torque transmission are also investigated. The test rig of the TBM cutter-head driving system was set up to validate the numerical method and the model of a cutter-head driving system, and the feasibility of the proposed numerical method for researching the extrication of the TBM cutter-head is verified.

Keywords: TBM, Hydro-viscous clutch, Explicit pressure equation, Extrication strategy

1 Introduction

A tunnel boring machine (TBM) is a kind of tunnel construction equipment that integrates rock mechanics, mechatronics, hydraulic control, and optical metrology. It is currently in high demand in many industrial applications, such as municipal transportation, water conservancy, and mining tunnel construction. However, TBM cutter-heads are often trapped by unstable rock during tunneling, and the conventional cutter-head driving system cannot supply enough torque to remove itself from the collapsed rock. As a result, the TBM has to stop working, and the losses including wasted time and money are huge.

The TB880E type of TBM by the Wirth Company utilizes hydraulic motors and double speed electric motors to drive the TBM head-cutter. The double speed electric motors are used for normal tunneling, while the hydraulic motors are used for supplying more power to realize cutter-head extrication from the surrounding rock, and these two driving chains are unable to work simultaneously. This type of TBM, however, is not fit for the different kinds of rock that are subject to the adjustable head-cutter speed, and this TBM has essentially been abandoned.

The variable-frequency driving mode of the TBM head-cutter has become mainstream, and the variable-frequency motor are appropriate for all cases, including normal and extrication cases. It is affirmed that this type of driving chain has significantly improved the energy-savings and driving efficiency. However, it is generally has insufficient torque capacity and a short duration

*Correspondence: hbxie@zju.edu.com
State Key Laboratory of Fluid Power & Mechatronic Systems, Zhejiang University, Hangzhou 310027, China

(approximately 1 min) of lasting extrication, which is mainly limited to the capacity of the variable-frequency controllers. In addition, because of the rigid join of parts in each driving chain, a serious impact may occur and cause unexpected damage to the mechanical system when motors start immediately during a fast extrication.

To relieve rigid impact and promote torque capacity during the extrication of the cutter-head, the hydro-viscous clutch (HVC) has recently been applied to the driving system of the TBM cutter-head by many researchers, and the inside structure and working principle of the HVC have been introduced [1–4]. Liao et al. [5–9] designed a new kind of cutter-head driving system which includes a flywheel and HVC in each cutter-head driving chain, and the popular variable-frequency method is still used. During normal tunneling, the friction disks of the HVC are completely engaged, and the flywheels are rotating. If the cutter-head is stuck, the friction disks of the HVC are first separated, then the flywheels are driven by motors at high speeds to store enough power, and the HVC disks are then controlled and joined to provide the cutter-head with more extricating torque. A new kind of cutter-head driving system structure with a HVC is also proposed [10–13], where the variable-frequency driving chain and the HVC driving chain are separate. Only the variable-frequency driving chains work under normal working conditions, while the HVC driving chains driven by ordinary AC motors are started synchronously with the variable-frequency driving chains under extrication conditions.

A large number of studies related to research on the extricating performance of cutter-head driving systems with an HVC in the TBM, have been reported. Liao et al. [14–17] established dynamic models of the HVC and film bearing capacity and performed simulations by integrating these models and other mechanical models in the AMESim software. Slightly different from Liao's method. Xie et al. [10] employed the original HVC model affiliated with the AMESim software to study extrication performance. They validated the feasibility and high efficiency of the HVC for TBM cutter-head extrication, but their models of the HVC were greatly simplified; hence, the calculating accuracy needs to be improved. Xie et al. [18–23] also adopted an approximate iteration algorithm based on the Navier–Stokes equations to obtain the analytical model for one friction pair in the HVC system, but there were inconsistencies in experimental results using the model.

In addition, Meng and Hou [24] numerically solved the transient Reynolds equations with centrifugal and squeeze effects in the HVC during speed regulation. Similar to Meng and Hou, Li et al. [25] not only numerically solved the corrected Reynolds equation but also took groove shapes and heat transfer into account, further investigating their influence on the engagement performances. Natsumeda and Miyoshi [26] and Berger et al. [27] took the centrifugal effects and squeeze effects of hydro-viscous film into account, and the former solved the Reynolds equations with the finite element method, while the latter used the finite difference method. However, their methods had the common limitation of failing to obtain accurate viscous torque with two friction disks.

Poncet et al. [28] proposed a modified Reynolds stress model (RSM) to investigate the mean structure of annular radial outflow in rotor-stator disks, where the one-point statistical model was used for establishing a Reynolds stress tensor to close momenta equations. The hydro-viscous film flows can also be solved with common numerical methods, such as the self-similar method [29] and the SIMPLE family of algorithms [30]; these methods have been widely employed for fluid computation. Generally, these methods require additional complicated mathematical techniques and computation time and are not suitable for quick computations of hydro-viscous film.

To study the extrication performance of the HVC in a cutter-head driving system, an accurate numerical method for calculating the working parameters of the HVC is presented, and an integrated model of the whole cutter-head driving system is established. The physical models are introduced in Section 2, and the mathematical models of the driving system are discussed in Section 3. In Section 4, the effects of different film thickness variations and the effects of throughflow rate on extricating torque are investigated. In the last section, the conclusions are drawn.

2 Physical Models

Similar to Xie's design [10] in Figure 1, the cutter-head driving system includes double driving chains: a variable-frequency driving chain driven by the variable-frequency (VF) motor and an HVC driving chain driven by the AC motor. During normal tunneling, only the variable-frequency driving chains are used and the HVC driving chain is not. For cutter-head extricating cases, the two driving chains are both employed to provide the cutter-head with enough rotating torque to overcome the resistance from the collapsed surrounding rock. In addition, the flywheels are utilized in the HVC driving chain to store mechanical energy to produce a greater amount of torque without any increase in the total driving power of the system. During this process, more rigid impact can be released with the cutter-head relying on the soft characteristics of the viscous film in the HVC.

The objective cutter-head driving system with the HVC is shown in Figure 2, and the HVC is designed to

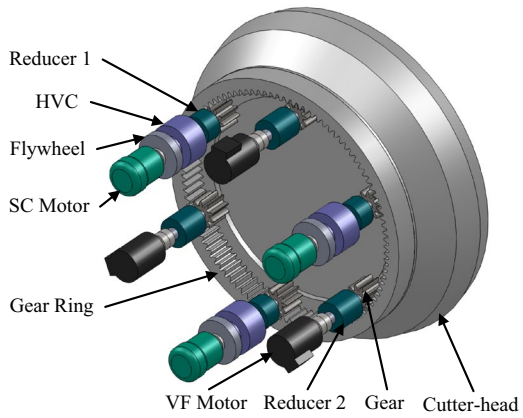

Figure 1 TBM cutter-head driving system with an HVC

have only one friction pair in this research. The driving system with the AC motor is used to supply power for extrication, and the load system with the brake is mainly used to simulate the load of real surrounding rock. The driving system with the servo motor is used to regulate film thickness. The flywheel is not studied in this research.

In Figure 2, the viscous lubricant oil with flow rate Q is continuously injected into the clearance of two disk, during which the film can form with inner radius R_i, outer radius R_o, and thickness h_0. The driving disk is driven by the AC motor with rotary speed ω_1 and driving torque M_1, and the viscous torque can be transferred from the driving disk to the driven disk through viscous stress of film to actuate the TBM cutter-head. The driven disk can move along the z-axis with speed V_a $(-\mathrm{d}h_0/\mathrm{d}t)$ with the servo motor and ball screw nut pushing, during which h_0 can be adjusted, and the coordinate plane o-r is always located on the driven disk surface. Meanwhile, the rotary speed of driven speed ω_2 can also be regulated by controlling the load from the brake. The two torque-speed detectors are used to measure the rotary speed and torque, and the film thickness h_0 is measured by the displacement detector. If the film thickness decreases, the viscous torque transferred to the cutter-head will increase, during which the extrication process of the cutter-head can be carried out. In addition, the thermal effect of film flow is not considered in this study because the imposed throughflow is enough to bring most heat out and keep the film temperature stable. The corresponding experimental device used is shown in Figure 3.

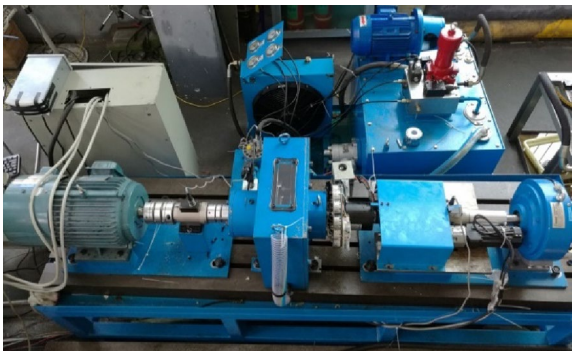

Figure 3 Experimental device for the cutter-head driving system

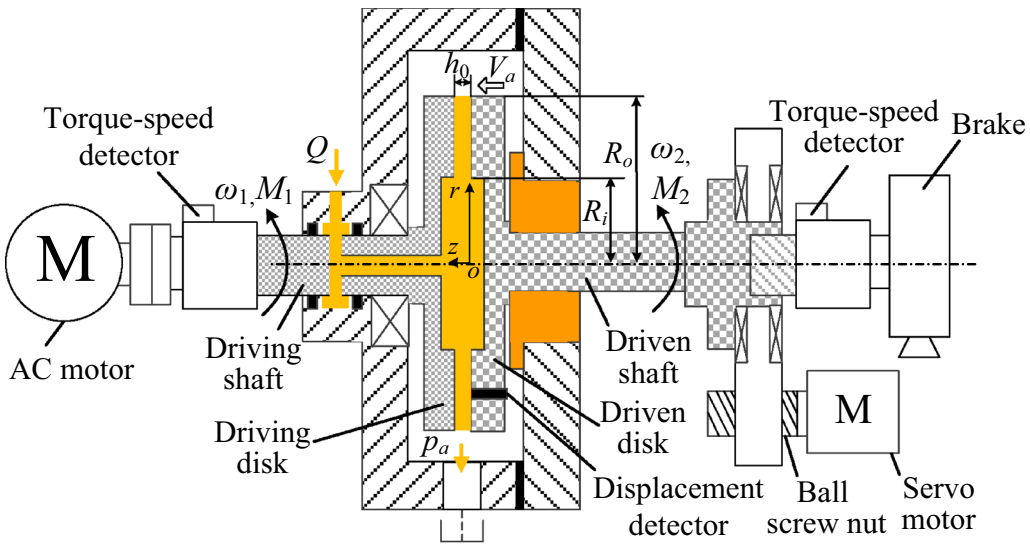

Figure 2 Sketch of the cutter-head driving system with the HVC

3 Mathematical Models

3.1 Models of Viscous Film

3.1.1 Governing Equations

The axisymmetric annular thin-film flow in Figure 2 is governed by the Navier–Stokes equations by rotating cylindrical polar coordinate (r, θ, z), and it is laminar because of its high viscosity and small thickness. The axial velocity component is negligible as its order of magnitude is lower than that of the other two components. Some usual assumptions in thin-film lubricant theory are applicable to this problem. To find accurate solutions, all inertial effects (including centrifugal effects and Coriolis effects) are also incorporated. Thus, the transient momentum equations for describing the thickness-changing film in the clearance of the two disks can be expressed as follows:

$$\frac{\partial v}{\partial t}+v\frac{\partial v}{\partial r}-\frac{1}{r}(u+r\omega)^2=-\frac{1}{\rho}\frac{\partial p}{\partial r}+\nu\frac{\partial^2 v}{\partial z^2}, \tag{1.1}$$

$$\frac{\partial u}{\partial t}+v\frac{\partial u}{\partial r}+\frac{vu}{r}+2\omega v=\nu\frac{\partial^2 u}{\partial z^2}, \tag{1.2}$$

$$\frac{1}{\rho}\frac{\partial p}{\partial z}=0, \tag{1.3}$$

where (u,v) are the velocity components in the circumferential and radial directions, respectively, $\omega=\omega_1-\omega_2$ is the relative rotary speed of two disks, p is the film pressure, $\nu=\mu/\rho$ is the kinematic viscosity, μ is the dynamic viscosity, and ρ is the fluid density. The no-slip and pressure-outlet boundary conditions of the flow film are

$$\left.\begin{aligned} z=0: u=r\omega_2, v=0,\\ z=h_0: u=r\omega_1, v=0,\\ r=R_o: p=p_a=0. \end{aligned}\right\} \tag{2}$$

In this research, integrating the radial velocity component across the film thickness yields the conservation equation

$$Q=2\pi r\int_0^{h_0} v\mathrm{d}z. \tag{3}$$

By integrating Eqs. (1.1) and (1.2), with respect to z, twice from 0 to z and taking boundary conditions (2) into account, the radial velocity component can be expressed in following form:

$$\begin{aligned} v=&\frac{1}{2\mu}\frac{\partial p}{\partial r}z(z-h_0)+\frac{1}{v}X(r,z)\\ &-\frac{1}{v}\left(1-\frac{z}{h_0}\right)X(r,0)-\frac{1}{v}\frac{z}{h_0}X(r,h_0), \end{aligned} \tag{4}$$

where

$$X(r,z)=\int_0^z\int_0^z\left(\frac{\partial v}{\partial t}+v\frac{\partial v}{\partial r}-\frac{1}{r}(u+r\omega)^2\right)\mathrm{d}z\mathrm{d}z. \tag{5}$$

Then the explicit expression of film pressure can be given by putting Eq. (4) into Eq. (3) and considering the pressure-outlet boundary condition:

$$p(r)=\frac{6\mu Q}{\pi h_0^3}\ln\frac{R_o}{r}+\frac{6\rho}{h_0^3}g(r), \tag{6}$$

where

$$g(r)=\int_r^{R_o}\left[h_0X(r,h_0)+h_0X(r,0)-2G(r)\right]\mathrm{d}r,$$

$$G(r)=\int_0^{h_0}X(r,z)\,\mathrm{d}z.$$

Thus, Eq. (6) can be used to solve film pressure directly because the pressure boundary condition has been involved in it, and computing time will be saved. In addition, the solving precision can also be guaranteed without and approximation in the procedure of deriving the pressure equation.

The viscous torque and film load capacity are as follows:

$$M=\int_{R_i}^{R_o}2\pi r^2\tau_{z\theta}\mathrm{d}r, \tag{7}$$

$$F=\int_{R_i}^{R_o}2\pi rp\,\mathrm{d}r, \tag{8}$$

where $\tau_{z\theta}=\mu\partial u/\partial z$ is the tangential component of viscous stress.

3.1.2 Numerical Method

Uniform mesh is used during the transient computation, and the dynamic mesh technique is used for time-varying film thickness. The momentum Eq. (1) are discretized with the finite volume method. The quadratic upstream interpolation for convective kinetics (QUICK) differencing scheme is employed while the backward differencing scheme is adopted for the time terms. The numerical integration method is used for calculating the film pressure, viscous torque, load capacity, and related intermediate variables. In addition, the successive over relaxation algorithm is used to solve the film parameters, and the error criterion of iterative convergence for each time step is:

$$\max_n \left(\max_{n}^{k=1\sim3} \left| \frac{\varphi_{kn}^m - \varphi_{kn}^{m-1}}{\varphi_{kn}^{m-1}} \right| \right) \le \varepsilon, \tag{9}$$

where n denotes the current time, m is the current number of iteration steps within current time step, and ϕ_k and $k=1$–3 represent three kinds of film parameters: radial velocity, azimuthal velocity, and film pressure. In each time step, the velocity components are computed and then substituted into Eq. (6) to solve for the film pressure. The tolerant error ε is 1×10^{-7}, and once the convergence is achieved, the iteration for the next time step starts.

Above all, this numerical method is proposed to substitute traditional implicit or semi-implicit pressure-linked equations by using a completely explicit pressure formula to avoid the internal iterations of the pressure term and greatly save computation time while also improving the computation accuracy of the HVC film parameters.

3.2 Models of Driving Side

The AC motor used in this research is an AC three-phase asynchronous motor whose rotating shaft is connected to the driving shaft of the HVC. Therefore, the dynamic model of the driving side can be described as

$$\begin{cases} M_{\mathrm{e}} = M_1 + c_1\omega_1 + J_1\frac{\mathrm{d}\omega_1}{\mathrm{d}t}, \\ n_p\omega_1 = \frac{\mathrm{d}\theta}{\mathrm{d}t}, \end{cases} \tag{10}$$

where M_{e} is the electromagnetic torque of the motor, c_1 is the coefficient of the viscous friction, θ is the rotating angle of the motor rotor, n_p is the number of pole pairs, and J_1 is moment of inertia for the driving side.

The AC three-phase asynchronous motor's electromagnetic torque can also be expressed as:

$$M_{\mathrm{e}} = \frac{n_p}{2}\boldsymbol{i}^{\mathrm{T}}\frac{\partial \boldsymbol{L}}{\partial\theta}\boldsymbol{i}, \tag{11}$$

where $\boldsymbol{i}$ is the motor current vector, and $\boldsymbol{L}$ is the motor inductance matrix, and in which

$$\frac{\partial \boldsymbol{L}}{\partial\theta} = \begin{bmatrix} \mathbf{0} & \frac{\partial \boldsymbol{M}_{sr}}{\partial\theta} \\ \frac{\partial \boldsymbol{M}_{rs}}{\partial\theta} & \mathbf{0} \end{bmatrix}, \tag{12}$$

and

$$\begin{aligned} \boldsymbol{M}_{\mathrm{sr}} &= \boldsymbol{M}_{\mathrm{rs}}^{\mathrm{T}} \\ &= M_{12}\begin{bmatrix} \cos\theta & \cos\left(\theta+\frac{2\pi}{3}\right) & \cos\left(\theta-\frac{2\pi}{3}\right) \\ \cos\left(\theta-\frac{2\pi}{3}\right) & \cos\theta & \cos\left(\theta+\frac{2\pi}{3}\right) \\ \cos\left(\theta+\frac{2\pi}{3}\right) & \cos\left(\theta-\frac{2\pi}{3}\right) & \cos\theta \end{bmatrix}, \end{aligned} \tag{13}$$

where M_{12} is the inductance when the winding axes of the rotator and stator coincide.

3.3 Models of Servo Driving System

In order to more accurately regulate the film thickness of the HVC, the servo motor shown in Figure 2 is utilized in combination with a reducer and ball screw nut. The dynamic equation of this mechanical transmission chain can be described as

$$T_2 = \frac{F_a PN}{2\pi} + J_s\frac{\mathrm{d}\omega_s}{\mathrm{d}t}, \tag{14}$$

where P is the screw lead, N is the reduction ratio of the servo reducer, ω_{s} is the rotary speed of the servo-motor shaft, and J_{s} is the equivalent moment of inertia acting on the motor shaft. In addition, F_{a} is the axial force on the servo motor containing the film load capacity F, load capacity of the circle region ($r<R_i$) F_c, and equivalent axial frictional force of moving parts F_f:

$$F_a = F + F_f, \tag{15}$$

$$F_c = \pi r^2 p_i, \tag{16}$$

where $F_c=\pi r^2 p_{i,}$ and p_i is the inlet pressure of the film. The servo motor is set at the velocity mode where the film thickness can be precisely regulated by the control method of the proportion integration differentiation (PID), and the film thickness can also be obtained with ω_{s} and the corresponding reduction ratios of the driving chain.

3.4 Models of Driven Side

When the cutter-head is stuck, the load torque M_{L} from the surrounding rock is the stiction torque which is also the maximum. Once the driven torque M_2 exceeds the stiction torque, the cutter-head begins to rotate and M_{L} becomes the sum of the Coulomb friction torque M_{C} and the viscous friction torque. The load torque can therefore be written as

$$M_L = \begin{cases} M_{\max}, & \omega_2=0, \\ M_C + c_2\omega_2, & \omega_2 > 0, \end{cases} \tag{17}$$

where c_2 is the coefficient of viscous friction. For the second stage of cutter-head extrication, the dynamic equation for the driven side is

$$J_2\frac{\mathrm{d}\omega_2}{\mathrm{d}t} = M_2 - M_L, \tag{18}$$

where J_2 is the moment of inertia of the driven side.

4 Validation and Results

4.1 Parameters of Cutter-Head Driving System

Integrating the relationship of the parameters and equations in Section 3, the logic relation of the subsystems

in the cutter-head driving system can be established. The parameter interrelations between the servo driving system, driving system (AC motor driving system), and driven system (load system) are shown in Figure 4.

Based on Figure 4, we can further investigate the extrication performance of the system with the physical parameters listed in Table 1. All of the mathematical models in Section 3 are programmed and computed using MATLAB R2012b.

4.2 Extrication Characteristics Under Different Strategies

Extrication is divided into three stages: the starting time of AC motor from 0 s to 2.0 s, the extrication of the cutter-head driving system from 2.0 s to 7.0 s, and the cutter-head maintains its working state from 7.0 s to 10.0 s. Three strategies regarding the variation in film thickness are investigated and compared in the extrication stage: positive parabola, linear, and negative parabola. Their expressions can be written as:

$$\begin{cases} h_p(t) = a_1 t^2 + b_1 t + c_1, & 2\ \text{s} \le t \le 7\ \text{s}, \\ h_l(t) = a_2 t + b_2, & 2\ \text{s} \le t \le 7\ \text{s}, \\ h_n(t) = a_3 t^2 + b_3 t + c_3, & 2\ \text{s} \le t \le 7\ \text{s}, \end{cases} \tag{19}$$

where $a_1 > 0$, and $a_3 < 0$. The film thickness h_0 decreases from 0.5 mm to 0.005 mm during this time, which has been shown in Figure 5. What should be emphasized is that because the boundary lubricant and full mechanical contact are not researched here, h_0 is set to be extremely small to approach the full mechanical contact of the two disks.

In Figure 6a, the cutter-head begins to get out of being stuck at 6.2 s, before which the driven torque M_2 is increasing, leading to the decrease in speed of AC motor ω_1. From 6.2 s to 7.0 s, the driven speed ω_2 is always increasing until to 47.4 rad/s, and M_2 also increases to the maximum value 25.5 N·m, while ω_1 declines further to 53.8 rad/s. For extrication characteristics of the linear strategy in Figure 6b, the time when cutter-head begins to rotate is 5.4 s. However, during the 5.4 s to 7.0 s period, the driven torque increases more slowly than in the negative parabolic strategy, and the maximum torque becomes 13.2 N·m at 7.0 s. Overall, the linear extrication process is similar to that under the negative parabolic strategy. In addition, as shown in Figure 6c, the results of the positive parabolic strategy are very different from the others. The cutter-head can overcome the load torque at 4.2 s, and the variation rate of M_2 is decreasing between 4.2 s and 5.3 s, although M_2 increases afterward. The driven torque M_2 has already reached its largest value at 5.3 s, and then it begins to drop and ω_1 increases. For the three cases, when the extrication ends, the film thickness is maintained at 0.005 mm after 7.0 s. Also, their driven torques M_2 all drop to the load torque 5.0 N·m, and the speed of the driven disk gradually increases to approach the driving speed. Furthermore, the maximum average relative error of torque between the numerical and experimental results is less than 5%, while the rotary speed error is less than 7%, which is acceptable and validates the numerical method.

Table 1 Main physical parameters

Parameter	Value	Unit
R_i	0.09	m
R_o	0.15	m
h_0	0.005–0.5	mm
ρ	872	kg/m^3
μ	0.027	Pa·s
Q	5	L/min
ω_1	0–74.5	rad/s
c_1, c_2	5.3×10^{-4}, 5.3×10^{-4}	N·m/(r/min)
n_p	4	–
M_{12}	0.01	H
J_1, J_2	0.093, 0.131	kg·m^2
P	2	mm
N	1/30	
M_{max}, M_C	8, 5	N·m

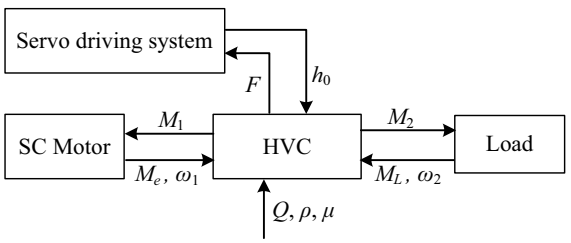

Figure 4 Parameter interrelations of cutter-head driving system

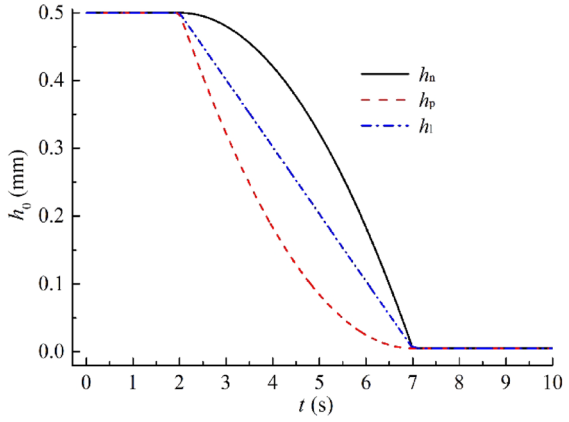

Figure 5 Different variations of film thickness during extrication

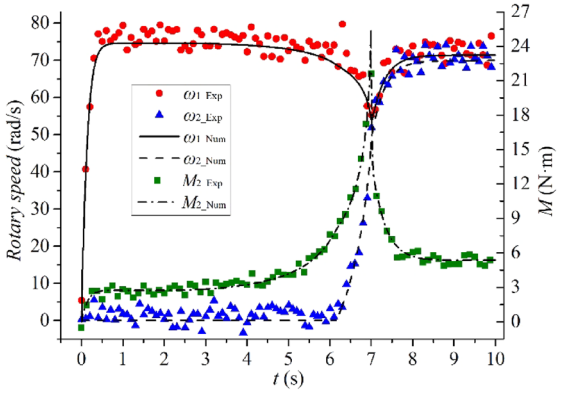

a Negative parabolic strategy.

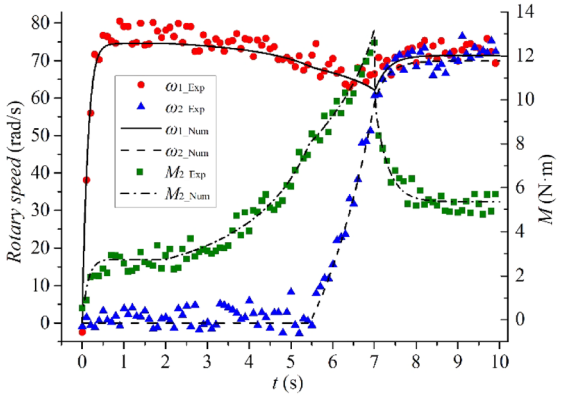

b Linear parabolic strategy.

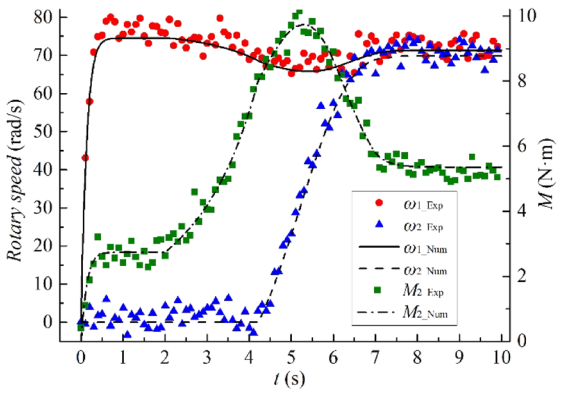

c Positive parabolic strategy.

Figure 6 Variations in rotary speed and driven torque

Comparing the extrication characteristics of the three strategies, we find that the extricating torque of the negative parabolic strategy is the largest and that of the positive parabolic strategy is the smallest. The positive and linear parabolic strategies cost 2.2 s and 3.5 s, respectively, to overcome the load torque, but this takes more than 4.0 s for the negative parabolic strategy. Hence, the extrication efficiency of the negative parabolic strategy may be lower.

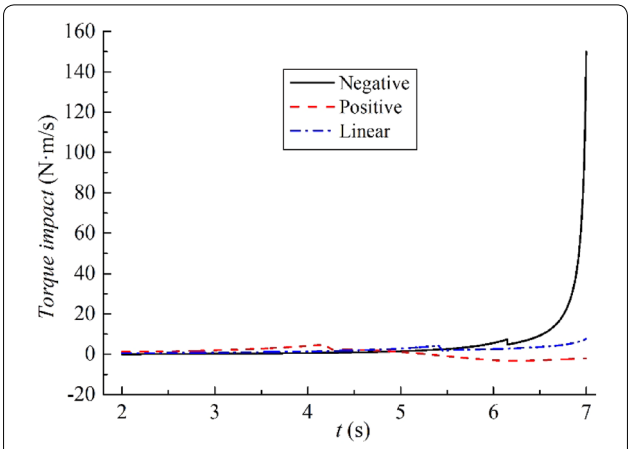

Figure 7 Torque impact under different strategies

The numerical torque impact under different strategies during the extrication period is shown in Figure 7, and the impact of the negative parabolic strategy increases sharply from 4.8 N·m/s to 150.1 N·m/s in about 0.85 s (from 6.153 s to the end of the time period). Namely, the torque impact is 170.9 N·m/s^2, which is the most serious. Correspondingly, we can calculate, based on Figure 6a, that the experimental impact is about 160 N·m/s^2 which is slightly less than the numerical impact (a relative error of 6.3% is acceptable) and mainly results from flexible coupling between the brake and torque-speed detector. As for the linear and positive parabolic strategies, their maximum impacts are 7.7 N·m/s and −3.3 N·m/s, respectively, which are much smaller than that of the negative parabolic strategy and their extrication process is smoother. Therefore, the linear and positive parabolic strategies can be adopted for extrication of the TBM cutter-head.

4.3 Effects of Throughflow Rate on Extrication Torque

As we have previously mentioned, cooled oil must be constantly imposed into the HVC to bring out the large quantities of heat coming from viscous dissipation and to keep film temperature at a low level. In other words, the larger the throughflow rate is, the less the film temperature rise will be. Then the viscosity reduction will be small, and a large amount of extrication torque can be ensured. Therefore, the effect of throughflow rate on extrication torque is investigated in this research. The viscosity-temperature effect is ignored to eliminate the influence of viscosity variation on the torque.

The output viscous torques with different Q under different extrication strategies are shown in Figure 8, where all the results are from numerical computations. It should be noted that before the cutter-head starts to rotate, a

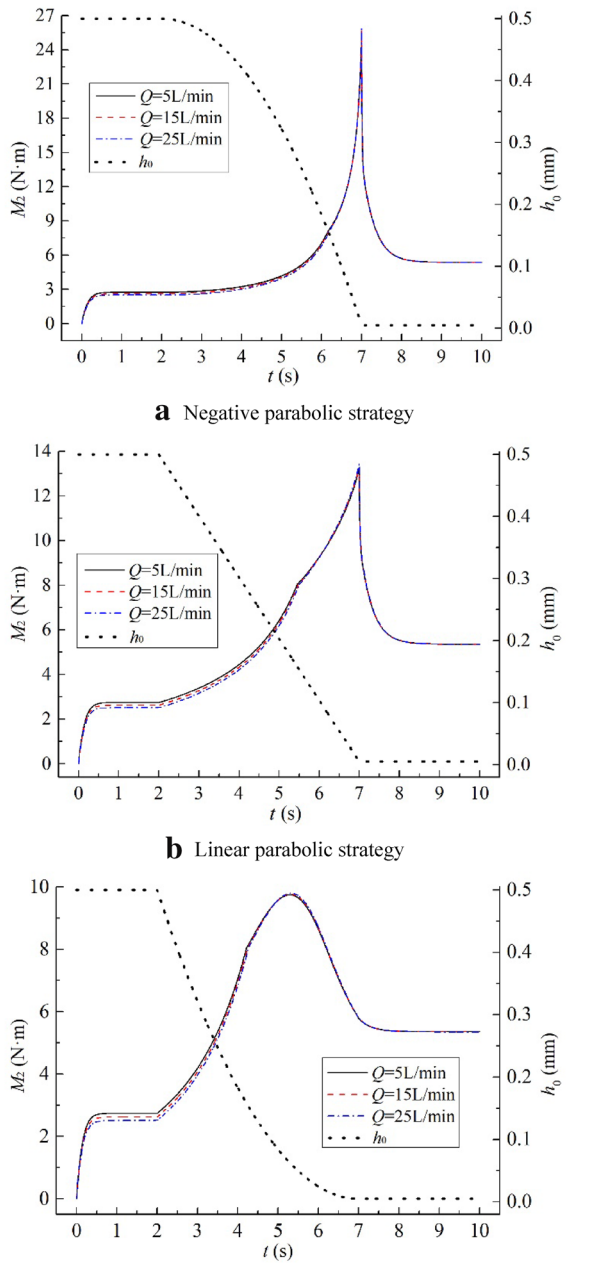

a Negative parabolic strategy

b Linear parabolic strategy

c Positive parabolic strategy

Figure 8 Variations of M_2 under different throughflow rate

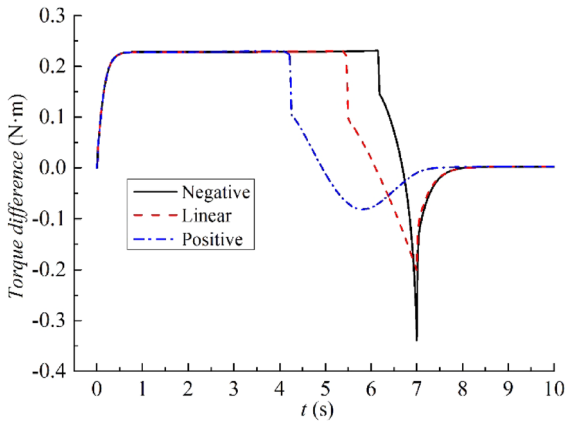

Figure 9 Driven torque differences between $Q=5$ L/min and $Q=25$ L/min under different strategies

larger throughflow rate Q reduces the extrication torque M_2. In addition, Figure 9 shows that the torque differences between 5 L/min and 25 L/min at $t=2.0$ s are all 0.228 N·m for the three strategies, while the differences increase to 0.231 N·m, 0.230 N·m, and 0.230 N·m, respectively, when the cutter-head starts, which indicates that the resistant effect from the throughflow becomes more apparent for smaller film thicknesses in the extrication process of a cutter-head when $\omega_2=0$. However, it can also be found from Figure 9 that the difference declines from the onset time of cutter-head rotation to 7.0 s for the negative and linear strategies, which means that the driven torque M_2 increases more quickly with a large Q than with a small Q. During the last stage of the two strategies when h_0 is invariant, the difference rises again even though ω_2 is still increasing. Eventually, M_2 when $Q=5$ L/min is larger than when $Q=25$ L/min, and their difference again remains constant. In contrast, for the positive extrication strategy, the torque difference decreases from 4.2 s to 5.8 s and rises from 5.8 s to 7.0 s rather than decreasing the entire time from 4.2 s to 7.0 s.

The torque variation induced by throughflow rate is not significant when film thickness h_0 is very small during the extrication of the cutter-head. Therefore, the throughflow rate imposed into the HVC can be increased to bring out more heat and improve extrication efficiency.

5 Conclusions

(1) A numerical method based on an explicit pressure-linked equation is proposed to study the extrication characteristics of a TBM cutter-head with the HVC applied. This method can not only save computation time but also improve computational accuracy of the HVC during the extrication.

(2) The extrication processes of the TBM cutter-head for three kinds of extrication strategies are analyzed and compared, and the linear strategy or positive parabolic strategy can be adopted due to their relatively high extrication efficiency and low rigid impact.

(3) The experiments corresponding to different extrication strategies are implemented. The results verify

the accuracy of the numerical method proposed in this paper.

(4) The influence of throughflow rate is different in different extrication stages, but the results reveal that the torque variation from throughflow rate is not significant during the extrication; therefore, throughflow can be increased to promote extrication efficiency.

Authors' Contributions

HX was in charge of the whole trial; HG wrote the manuscript and was in charge of the whole analysis; HY revised the final manuscript. All authors read and approved the final manuscript.

Authors' Information

Huasheng Gong, born in 1990. He received his PhD degree from *State Key Laboratory of Fluid Power & Mechatronic Systems, Zhejiang University, China*, in 2019. His research interests include hydro-viscous transmission and hydraulic control.

Haibo Xie received his PhD degree from *Zhejiang University, China*, in 2004, and now works as a professor at *State Key Laboratory of Fluid Power and Mechatronic Systems, Zhejiang University, China*. His current research interests include mobile hydraulic control systems and components, tunneling boring machine driving technique.

Huayong Yang, academician of the Chinese Academy of Engineering, received his PhD degree from *Bath University, UK*, in 1988, and now works as a professor at *State Key Laboratory of Fluid Power and Mechatronic Systems, Zhejiang University, China*. His current research interests include hydraulic systems and components.

Competing Interests

The authors declare that they have no competing interests.

Funding

Supported by Major State Basic Research Development Program of China (973 Program, Grant No. 2013CB035400), National Natural Science Foundation of China (Grant Nos. 51275451, 51575476), and Science Fund for Creative Research Groups of National Natural Science Foundation of China (Grant No. 51221004).

Received: 13 February 2019 Accepted: 4 November 2019
Published online: 05 December 2019

References

[1] J Y Jang, M M Khonsari. Thermal characteristics of a wet clutch. *Journal of Tribology*, 1999, 121(3): 610-617.

[2] A P Ompusunggu, P Sas, H Van Brussel. Modeling and simulation of the engagement dynamics of a wet friction clutch system subjected to degradation: An application to condition monitoring and prognostics. *Mechatronics*, 2013, 23(6): 700-712.

[3] M Daliri, D Jalali-Vahid. Investigation of combined effects of rotational inertia and viscosity-pressure dependency on the squeeze film characteristics of parallel annular plates lubricated by couple stress fluid. *Journal of Tribology*, 2015, 137(3): 031702-031702-6.

[4] T C Jen, D J Nemecek. Thermal analysis of a wet-disk clutch subjected to a constant energy engagement. *International Journal of Heat and Mass Transfer*, 2008, 51(7-8): 1757-1769.

[5] X P Liao, G F Gong, X B Peng, et al. Jam breakout characteristic of tunnel boring machine based on hydro-viscous drive mechanism. *Journal of Zhejiang University (Engineering Science)*, 2016(05): 902-912. (in Chinese)

[6] C C Sun, G F Gong, F Wang, et al. Single neuron adaptive PID control for hydro-viscous drive clutch. *Proceedings of the 12th IEEE/ASME International Conference on Mechatronic and Embedded Systems and Applications*, Auckland, New Zealand, August 29-31, 2016: 1-4.

[7] X P Liao, G F Gong, H Wang, et al. Dynamic performance of hydro-viscous drive clutch with double-piston. *Transactions of the Chinese Society for Agricultural Machinery*, 2014, 45(7): 1-6. (in Chinese)

[8] X P Liao, G F Gong, T Y Zhou, et al. Design and characteristic of lubricating oil chamber of hydro-viscous drive clutch. *Journal of Drainage and Irrigation Machinery Engineering*, 2014(12): 1062-1067. (in Chinese)

[9] W Q Wu, Z Xiong, J Hu, et al. Application of CFD to model oil-air flow in a grooved two-disc system. *International Journal of Heat and Mass Transfer*, 2015, 91: 293-301.

[10] H B Xie, X Hong, Y Zhao, et al. Application of hydro-viscous driver in TBM cutter-head driving technology. *Journal of Mechanical Engineering*, 2014, 21: 69-75. (in Chinese)

[11] X Hong. *TBM cutter-head driver scheme and test bench related design*. Zhejiang University, 2014. (in Chinese)

[12] Y Zhao, X Hong. Simulation research of breakout process of TBM cutter-head driver. *Machine Tool & Hydraulics*, 2014, 42(19): 123-126. (in Chinese)

[13] Y Zhao, X Hong. Development and key technologies of TBM cutter-head driver system. *Machine Tool & Hydraulics*, 2014 (12): 64-67. (in Chinese)

[14] X P Liao, G F Gong, C C Sun, et al. Dynamic engagement performance of hydro-viscous clutch based on AMESim. *Transactions of the Chinese Society for Agricultural Machinery*, 2016(06): 324-332. (in Chinese)

[15] X P Liao. *Study on the jam breakout technology of tunnel boring machine cutterhead driving system based on hydro-viscous coupling mechanism*. Zhejiang University, 2016. (in Chinese)

[16] T Y Zhou. *Research on the getting-out-of-jam ability of TBM based on hydro-viscous clutch*. Zhejiang University, 2015. (in Chinese)

[17] T Y Zhou, G F Gong, X P Liao, et al. Analysis on the oil film uniformity of hydro-viscous drive frictionpairs. *Journal of Harbin Engineering University*, 2015(07): 954-958. (in Chinese)

[18] H B Xie, H S Gong, L Hu, et al. Improving the extricating performance of TBM cutter-head driving system with hydro-viscous clutch. *Proceedings of the 12th IEEE/ASME International Conference on Mechatronic and Embedded Systems and Applications*, Auckland, New Zealand, August 29-31, 2016: 1-7.

[19] H B Xie, H S Gong, L Hu, et al. Coriolis effects on torque transmission of hydro-viscous film in parallel disks with imposed throughflow. *Tribology International*, 2017, 115: 100-107.

[20] H S Gong, H B Xie, L Hu, et al. Combined effects of Coriolis force and temperature-viscosity dependency on hydro-viscous transmission of rotating parallel disks. *Tribology International*, 2018, 117: 168-173.

[21] H S Gong. *Research on the Key Technologies of hydro-viscous transmission for cutter-head extrication of hard rock tunnel boring machine*. Zhejiang University, 2019. (in Chinese)

[22] H S Gong, H B Xie, L Hu, et al. Effects of groove orientation on transmission characteristics of hydro-viscous film in the parallel-disk system. *Proceedings of the Institution of Mechanical Engineers, Part J: Journal of Engineering Tribology*, 2019: 1350650119858238.

[23] H B Xie, H S Gong, H Y Yang. Research on the soft-starting characteristics of wet clutches in TBM cutter-head driving system. *Intelligent Robotics and Applications*, 2015: 456-468.

[24] Q R Meng, Y F Hou. Effect of oil film squeezing on hydro-viscous drive speed regulating start. *Tribology International,* 2010, 43(11): 2134-2138.

[25] M Li, M M Khonsari, D M C McCarthy, et al. Parametric analysis for a paper-based wet clutch with groove consideration. *Tribology International*, 2014, 80: 222-233.

[26] S Natsumeda, T Miyoshi. Numerical simulation of engagement of paper based wet clutch facing. *Journal of Tribology*, 1994, 116(2): 232-237.

[27] E J Berger, F Sadeghi, C M Krousgrill. Finite element modeling of engagement of rough and grooved wet clutches. *Journal of Tribology*, 1996, 118(1): 137-146.

[28] S Poncet, R Schiestel, M P Chauve. Centrifugal flow in a rotor-stator cavity. *Journal of Fluids Engineering*, 2005, 127(4): 787-794.

[29] I V Shevchuk. A self-similar solution of Navier–Stokes and energy equations for rotating flows between a cone and a disk. *High Temperature*, 2004, 42(1): 104-110.

[30] H K Versteeg, W Malalasekera. *An introduction to computational fluid dynamics: the finite volume method*. Pearson Education, 2007.